

Defects in Microelectronic Materials and Devices

Edited by

**Daniel M. Fleetwood • Sokrates T. Pantelides
Ronald D. Schrimpf**



CRC Press

Taylor & Francis Group

Boca Raton London New York

CRC Press is an imprint of the
Taylor & Francis Group, an **informa** business

Figure on cover: Z-contrast image of a silicon-silicon dioxide-hafnium dioxide structure showing an isolated Hf atom in the SiO₂ interlayer (image courtesy of K. Van Benthem and S. J. Pennycook). The expanded image is an electron density plot for this structure (courtesy of A. G. Marinopoulos and S. T. Pantelides).

CRC Press
Taylor & Francis Group
6000 Broken Sound Parkway NW, Suite 300
Boca Raton, FL 33487-2742

© 2009 by Taylor & Francis Group, LLC
CRC Press is an imprint of Taylor & Francis Group, an Informa business

No claim to original U.S. Government works
Printed in the United States of America on acid-free paper
10 9 8 7 6 5 4 3 2 1

International Standard Book Number-13: 978-1-4200-4376-1 (Hardcover)

This book contains information obtained from authentic and highly regarded sources. Reasonable efforts have been made to publish reliable data and information, but the author and publisher cannot assume responsibility for the validity of all materials or the consequences of their use. The authors and publishers have attempted to trace the copyright holders of all material reproduced in this publication and apologize to copyright holders if permission to publish in this form has not been obtained. If any copyright material has not been acknowledged please write and let us know so we may rectify in any future reprint.

Except as permitted under U.S. Copyright Law, no part of this book may be reprinted, reproduced, transmitted, or utilized in any form by any electronic, mechanical, or other means, now known or hereafter invented, including photocopying, microfilming, and recording, or in any information storage or retrieval system, without written permission from the publishers.

For permission to photocopy or use material electronically from this work, please access www.copyright.com (<http://www.copyright.com/>) or contact the Copyright Clearance Center, Inc. (CCC), 222 Rosewood Drive, Danvers, MA 01923, 978-750-8400. CCC is a not-for-profit organization that provides licenses and registration for a variety of users. For organizations that have been granted a photocopy license by the CCC, a separate system of payment has been arranged.

Trademark Notice: Product or corporate names may be trademarks or registered trademarks, and are used only for identification and explanation without intent to infringe.

Library of Congress Cataloging-in-Publication Data

Fleetwood, Daniel.
Defects in microelectronic materials and devices / Daniel Fleetwood, Sokrates T. Pantelides, and Ronald D. Schrimpf.

p. cm.
Includes bibliographical references and index.
ISBN 978-1-4200-4376-1 (alk. paper)
1. Microelectronics--Materials--Testing. 2. Metal oxide semiconductor field-effect transistors--Testing. 3. Integrated circuits--Defects. I. Pantelides, Sokrates T. II. Schrimpf, Ronald Donald. III. Title.

TK7871.F5485 2008
621.381--dc22

2008018722

Visit the Taylor & Francis Web site at
<http://www.taylorandfrancis.com>

and the CRC Press Web site at
<http://www.crcpress.com>

8

From 3D Imaging of Atoms to Macroscopic Device Properties

S.J. Pennycook, M.F. Chisholm, K. van Benthem, A.G. Marinopoulos,
and Sokrates T. Pantelides

CONTENTS

8.1	Introduction	259
8.2	Scanning Transmission Electron Microscopy	261
8.3	Theoretical Microscope	267
8.4	Structure and Properties of Si/SiO ₂ /HfO ₂ Gate Stacks by Aberration-Corrected STEM and Theory	271
8.5	Future Directions	276
	Acknowledgments	277
	References.....	278

8.1 Introduction

The quest for smaller, faster semiconductor devices is rapidly approaching the so-called “end of the roadmap” for silicon-based devices, in which the thickness of the gate oxide is becoming too small to maintain the macroscopic properties of that mainstay of the semiconductor industry, SiO₂. As the thickness approaches the size of the intrinsic ring structure of SiO₂, the electronic integrity of the gate oxide becomes compromised, and undesirable characteristics such as leakage and dielectric breakdown cannot be managed effectively. This situation is the driver for the search for alternative, high dielectric constant (high-*k*) gate structures. The introduction of new materials to augment a thin SiO₂ interlayer raises the possibility of new kinds of impurities entering either SiO₂ or the Si substrate, and that dopant atoms may enter new configurations, adversely affecting macroscopic device properties. It therefore becomes very valuable to be able to characterize these nanometer scale device structures with probes that are sensitive to individual atoms, ideally in three dimensions. At the same time, the ability to determine local electronic structure with similar resolution and sensitivity would reveal any local defect states introduced into the band gap as a result of these impurity or dopant atoms. In conjunction with theoretical calculations of electronic structure, it would then become possible to link the atomic-scale characterization of actual device structures to their macroscopic

characteristics, and thus to find the true atomic origins of, for example, high leakage current or low mobility.

In this chapter, we describe the latest advances in aberration-corrected scanning transmission electron microscopy (STEM), which have in the last few years brought this vision to a practical possibility. The ability to correct for the primary aberrations of electron lenses represents a revolution in the field of electron microscopy. The rate of instrumental advance today is faster than at any time since the invention of the electron microscope in the 1930s, as shown in Figure 8.1 [1]. Aberrations occur inevitably in round lenses, as a result of physics, and not only from imperfections, as was recognized by Scherzer over 70 years ago [2]. The spherical aberration of the simple round lens has limited electron microscope resolution for most of its history, as was appreciated by Feynman in his 1959 lecture, [3] "There's Plenty of Room at the Bottom," where he explicitly called for a 100-fold improvement in resolution by overcoming spherical aberration, "why must the field be symmetric?" Designs for aberration correctors have existed for over 60 years [4], but they require multipole lenses, which makes such schemes enormously complex. It was not until the era of the fast computer and the efficient detection of the charge-coupled device that it has become practically possible to measure aberrations with the necessary sensitivity, ~ 1 part in 10^7 , and to control all the multipoles to the required accuracy. Focusing, or tuning, the aberration corrector involves optimization in a space of 40 or more dimensions, which has proved to be beyond human capability. Therefore, it is not so surprising that the successful correction of aberrations in electron microscopy has had to wait for the computer age.

Now, aberration correction has been successfully achieved both in the conventional transmission electron microscope (TEM) [5] and in the STEM [6]. In the STEM, direct imaging of a crystal lattice has been achieved at subangstrom resolution; see Figure 8.2 [7]. But aberration correction brings more than just a factor of 2 or 3 in resolution. As shown, in the STEM it also brings a greatly improved signal-to-noise ratio, resulting in the ability to image individual Hf atoms inside the nanometer-wide gate oxide of an advanced dielectric device structure [8]. Furthermore, since the lens aperture is much wider after

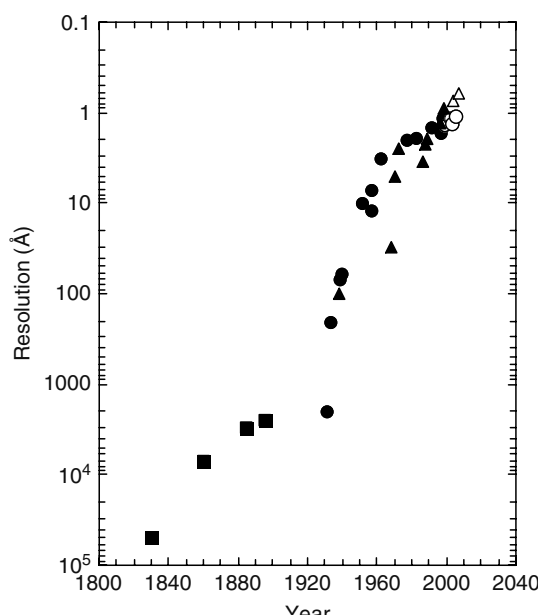
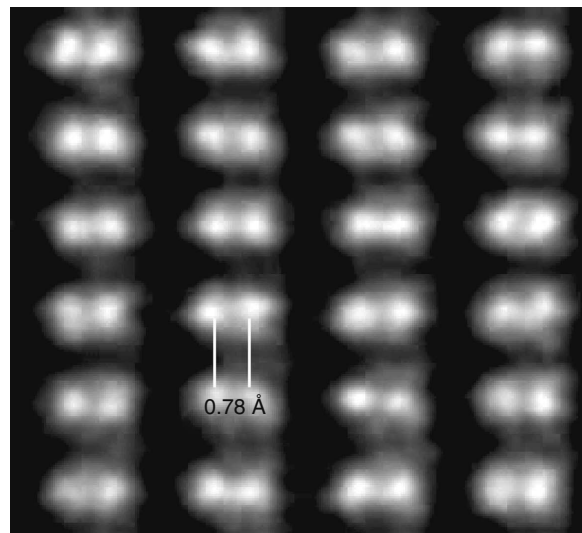


FIGURE 8.1

Evolution of resolution; squares represent light microscopy, circles TEM, triangles STEM, solid symbols before aberration correction, open symbols after correction. (After Rose, H., *Ultramicroscopy*, 56, 11, 1994. With permission.)

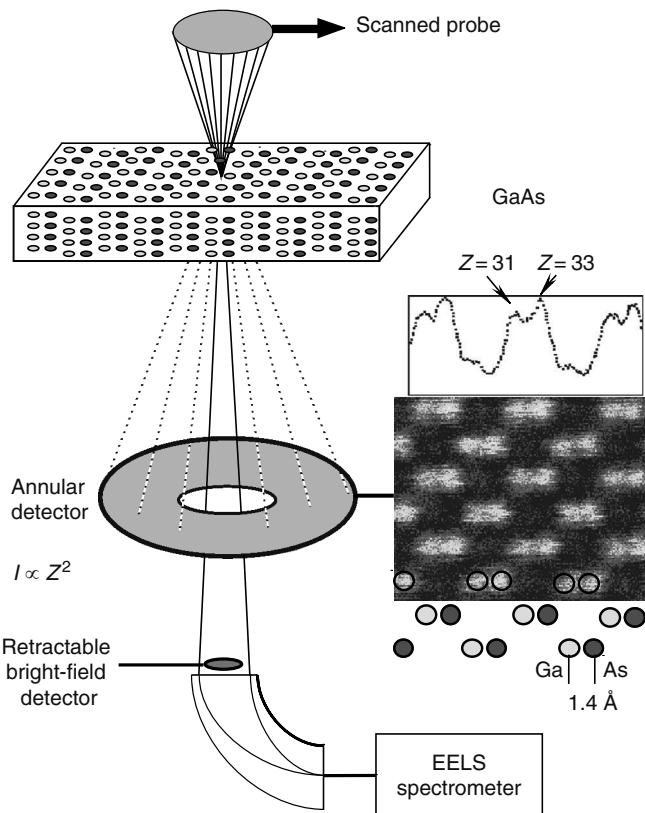
**FIGURE 8.2**

Direct imaging of a Si crystal in the $<112>$ projection showing resolution of pairs of Si columns just 0.78 \AA apart, obtained with a VG Microscopes HB603U dedicated STEM equipped with a Nion aberration corrector. (Adapted from Nellist, P.D. et al., *Science*, 305, 1741, 2004. With permission.)

aberration correction, the depth of field is much smaller, and it becomes possible to locate atoms in three dimensions to a precision better than 1 nm in depth and 0.1 nm in lateral position [9,10]. Three-dimensional mapping of heavy atoms inside SiO_2 has become possible, and in principle, three-dimensional spectroscopy should be feasible. With this level of sensitivity, new insights are available into the microscopic defects in device structures and their influence on device characteristics. From such knowledge, properties can be calculated from first principles, enabling the determination of the atomic-scale defects responsible for macroscopic device properties such as leakage and mobility, leading to improved device design.

8.2 Scanning Transmission Electron Microscopy

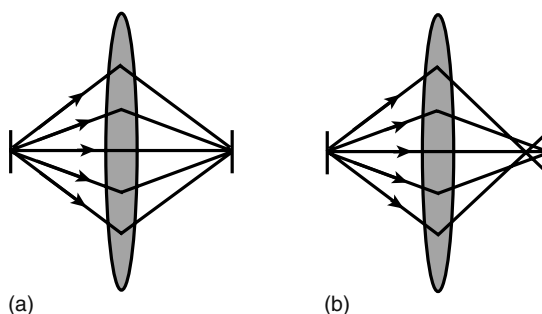
Figure 8.3 shows a schematic diagram of a STEM. As in any scanning microscope, the image is built up sequentially, pixel by pixel, as the probe is scanned across a specimen, and a variety of signals can be detected to form an image. The two most important imaging signals are the transmitted electron signal, which gives a bright-field image, and the scattered electron signal, which gives a dark-field signal. These two images are complementary, giving quite different information about the sample. The bright-field image can be arranged to give a high-resolution phase contrast image just as seen in a conventional TEM [11]. A phase contrast image is a coherent image formed by interference between diffracted beams, and fringes in the image can be black or white depending on whether the interference is constructive or destructive, which depends sensitively on parameters such as specimen thickness and microscope focus. Consequently there can be significant ambiguity on where the atoms actually are, and direct interpretation of atomic structure from the image is generally not feasible. Instead, simulations of trial structures are usually performed.

**FIGURE 8.3**

Schematic of a STEM. A finely focused probe is scanned over a specimen and an image is built up point-by-point. Simultaneous bright-field and dark-field images are possible or the bright-field detector may be replaced with an electron spectrometer to provide atomically resolved spectroscopic imaging. (Adapted from Pennycook, S.J. et al., *Philos. Trans. R. Soc. London, Ser. A*, 354, 2619, 1996. With permission).

The annular (or high-angle annular) detector gives an image of quite different character, which is essentially an atomic-resolution map of the specimen's scattering power [12,13]. The intensity of electrons scattered by a specimen is approximately proportional to its mean square atomic number (Z), and also its thickness, at least up to a few tens of nanometers, by which time most of the beam has been scattered and the image saturates. The annular dark-field (ADF) image is therefore an incoherent image, which has a directly interpretable relationship between object and image, just like the image formed with an optical camera or projector. Because of these characteristics, the image is often referred to as a Z -contrast image. High- Z atoms can be directly distinguished in the image, and unexpected configurations can be immediately apparent, properties that have been very useful in identifying many unexpectedly complex defect arrangements at semiconductor interfaces [14–20]. Until recently, however, Z -contrast images have been substantially noisier than the phase contrast images obtained in conventional TEM. This is because only a small current can be focused into a small spot, which is then scanned sequentially over the field of view. Conventional TEM images are obtained with a broad, high-current beam, with all image points being imaged in parallel.

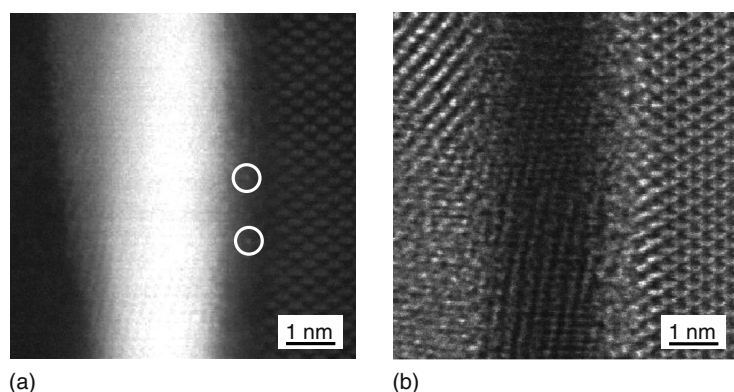
In recent years major improvements in STEM instrumentation have occurred, including the successful incorporation of high-resolution STEM capabilities into commercial

**FIGURE 8.4**

Schematic showing the action of spherical aberration in overfocusing high-angle rays. (Adapted from Varela, M. et al., *Annu. Rev. Mater. Res.*, 539, 2005, With permission.)

microscope columns with efficient detectors [21]. In particular, the development of aberration correctors has dramatically improved STEM performance [22,23]. For around 60 years, spherical aberration has been the major limitation to microscope resolution. As shown in Figure 8.4, spherical aberration is the tendency for high-angle rays passing through the lens to be overfocused, meaning that beyond a certain maximum aperture they are not usefully contributing to the focused spot but produce an extended tail in the image. Thus, spherical aberration results in a maximum effective aperture. Microscope resolution is proportional to λ/θ , where λ is electron wavelength and θ is the semiangle of the objective lens. By correcting for the lowest-order aberrations of the objective lens, the aperture can be opened up by a significant factor of between 2 and 3, which translates directly into improved resolution. However, not only has reducing the probe size enhanced the resolution, but also, the same current can now be focused into a smaller probe, giving a vastly higher peak intensity in the narrower beam. As a result, the signal-to-noise ratio in aberration-corrected images is greatly improved compared to uncorrected images, and the sensitivity to individual high-Z atoms is enormously increased [24–36].

Another key advantage of the STEM is that multiple detectors can be used to obtain complementary images with pixel-to-pixel correlation. Simultaneously acquired bright-field and dark-field images can be directly compared, although the optimum focus for each is slightly different so that a focal series of images may be necessary for quantitative work [37]. Figure 8.5 shows simultaneously acquired, aberration-corrected phase- and

**FIGURE 8.5**

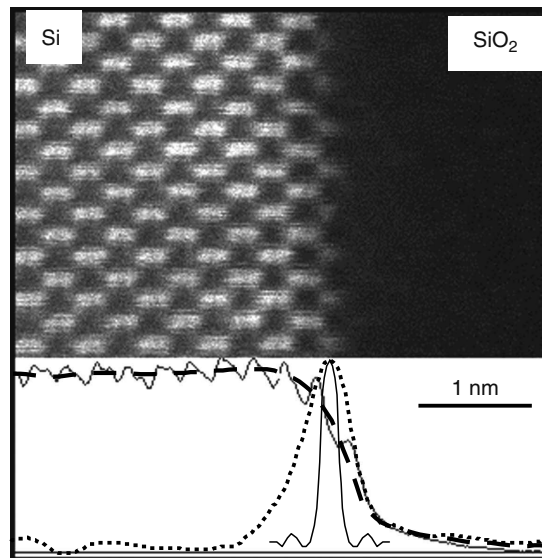
Simultaneously acquired (a) Z-contrast and (b) phase contrast images of a poly-Si/HfO₂/SiO₂/Si gate dielectric structure obtained with the aberration-corrected HB603U. (Adapted from Rashkeev, S.N. et al., *Microelectron. Eng.*, 80, 416, 2005; van Benthem, K., Rashkeev, S.N., and Pennycook, S.J., in *Characterization and Metrology for ULSI Technology*, American Institute of Physics, Richardson, TX, 2005, 79. With permission.)

Z-contrast images of a poly-Si/HfO₂/SiO₂/Si gate dielectric structure in which the different characteristics are very clear [38,39]. In the phase contrast image, the SiO₂ shows the speckle pattern typical of an amorphous material, caused by random interference effects within the structure, and the crystalline regions show lattice fringes. The Z-contrast image is dominated by the high scattering power of the HfO₂ ($Z = 72$ for Hf compared to 14 for Si and 8 for O). In the thin gate oxide layer there are small bright spots visible that represent single stray Hf atoms [8]. These are not detectable in the phase contrast image.

The exact position of the Si/SiO₂ interface is difficult to determine from the phase contrast image without extensive simulations, and it has therefore been proposed that microscopic measurements of dielectric layer thickness be determined from intensity traces across the Z-contrast images [40]. The incoherent nature of the Z-contrast image makes it reasonably immune to the influence of specimen thickness and interface roughness. An incoherent image is given by a mathematical convolution of a specimen object function with a resolution function of the optical instrument. In the case of ADF STEM, the resolution function is the intensity profile of the scanning probe, which is convoluted with the specimen scattering power. A useful concept is that of an effective probe, which is the probe profile integrated through the thickness of the specimen. In a crystal aligned to a major zone axis, the probe can channel along the columns. At the same time some intensity is scattered to high angles leading to probe broadening. In the amorphous oxide there is no channeling, but beam broadening remains. Because of the change in beam channeling, the effective probe will change somewhat as it is scanned across the Si/SiO₂ interface. However, these effects are generally small and normally ignored. The method proposed for thickness determination assumes the same effective probe in the crystal and in the oxide. For any radially symmetric probe profile, a convolution with a step function (for example, the abrupt change in intensity from Si to SiO₂) will lead to a blurring of the image intensity, with the point of inflection locating the interface. Hence, differentiating the intensity trace will regenerate the form of the effective probe. If now the interface has structural roughness, this will further broaden the intensity profile. However, the point of inflection will remain as the mean interface position, which is why the method is relatively immune to details of the specimen and microscope parameters.

The above procedure is illustrated in Figure 8.6. Differentiating the ADF intensity profile gives a peak at the interface position. Note, however, that the derivative trace is somewhat asymmetric. This illustrates the different channeling conditions on either side of the interface, and is indicative of the potential errors in the method. Also, the width of the derivative peak, $\sim 5 \text{ \AA}$, is much broader than the width of the probe, which is definitely of the order of 1.3 \AA , since it is resolving the Si dumbbell separation at 1.26 \AA . This is probably mostly due to interfacial roughness; however, even abrupt interfaces typically show a transition in intensity that is broader than expected from a simple convolution model. Such behavior is not predicted even by sophisticated image simulations. The problem is an unexplained background intensity in the images, which is higher for higher-Z materials, and the background intensity does not change abruptly across the interface. This issue is often referred to as the Stobbs factor, and is yet to be resolved [41].

Perhaps the most important simultaneous signals in STEM are obtained by replacing the bright-field detector with an efficient, parallel detection, electron spectrometer. Then, it becomes possible to use the ADF image to locate atomic planes or columns and to perform spectroscopy from specific columns selected from the image. The first atomically resolved spectroscopic analysis was demonstrated in 1993, in which a characteristic Co edge was measured plane-by-plane across a CoSi₂/Si interface [42]. The drop in measured Co concentration in moving from the last plane of the silicide to the first plane of the Si well exceeded the 50% points required to demonstrate atomic resolution. Later,

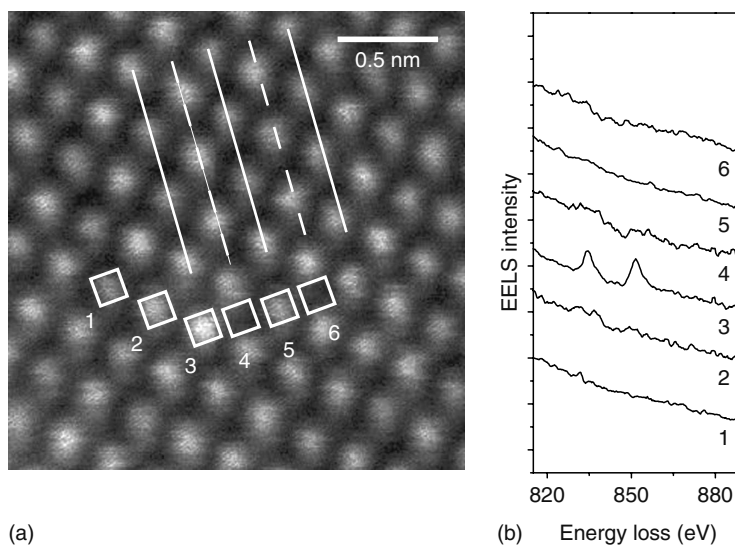
**FIGURE 8.6**

Z-contrast image of an Si-SiO₂ interface obtained with the uncorrected HB603U STEM. Its probe size of about 0.13 nm is still sufficiently small to resolve the Si dumbbells. A vertically averaged line trace (grey) is fitted with a smooth curve (dashed line), differentiated (dotted line), and the width can then be compared to the theoretically calculated probe profile (solid line). Reasons for the increased interface width can be interfacial roughness, and also probe broadening effects. (Reproduced from Diebold, A.C. et al., *Microsc. Microanal.*, 9, 493, 2003. With permission.)

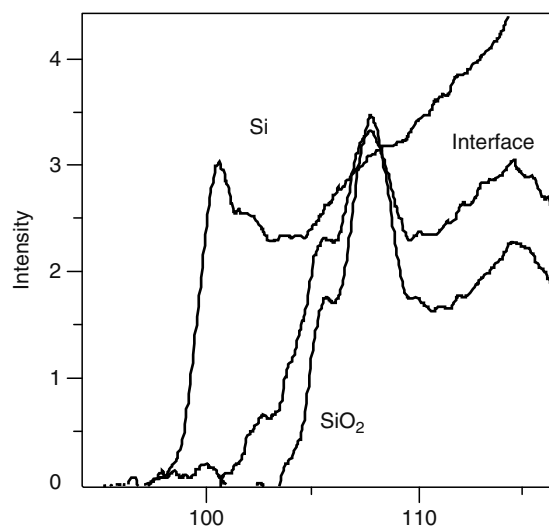
column-by-column spectroscopy became common [43–48], but recently, with the incorporation of aberration correctors into STEM columns, the improvements have become even more spectacular. First was the spectroscopic identification of an individual atom inside a bulk solid as shown in Figure 8.7, [49] and second, the recent achievement of true, two-dimensional atomic-resolution maps [50], as opposed to point spectra obtained from columns chosen from the Z-contrast image, both achievements due to the higher signal levels available after aberration correction.

Not only does electron energy loss spectroscopy (EELS) provide compositional information from the energies of characteristic absorption edges, but also the fine structure on those edges gives information on local electronic structure in a similar manner to x-ray absorption spectroscopy (XAS). Figure 8.8 shows spectra characteristic of bulk Si and SiO₂, and of the (rough) interface between them which shows additional peaks due to suboxide bonding [51]. STEM and EELS have developed into a powerful tool for the atomic and electronic characterization of interfaces in device structures [52–59]. Compared with XAS, EELS has the benefit of spatial resolution at the atomic level, and can probe changes that occur as the probe is moved across an interface, whereas XAS provides an average measurement. The problem, as always, is that EELS has poorer count statistics and so quantitative analysis is always limited by signal-to-noise.

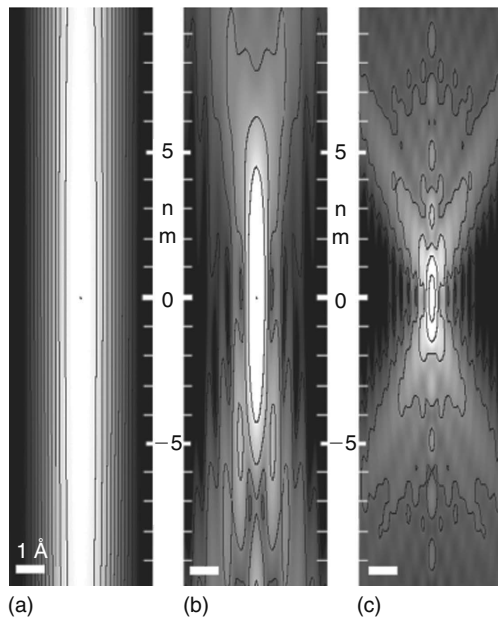
Whereas the motivation for aberration correction was primarily the resolution, implicitly the lateral resolution, a somewhat unanticipated advantage has been the gain in depth resolution, which is given by $2\lambda/\theta^2$. So a factor of 2 or 3 improvement in the transverse resolution brings also a factor of 4–9 in depth resolution. We have moved from a situation where the depth of field of the microscope is typically greater than the specimen thickness (the image is a projection of the specimen) to a situation where the depth of field is usually

**FIGURE 8.7**

Spectroscopic identification of a single La atom in a column of Ca in the perovskite CaTiO_3 . (a) Z-contrast image of CaTiO_3 showing traces of the CaO and TiO_2 {100} planes as solid and dashed lines, respectively. A single La dopant atom in column 3 causes this column to be slightly brighter than other Ca columns, and EELS shows a clear $\text{La M}_{4,5}$ signal (b). Moving the probe to adjacent columns gives reduced or undetectable signals. Results obtained using a VG Microscopes HB501UX STEM equipped with a Nion aberration corrector. (Adapted from Varela, M. et al., *Phys. Rev. Lett.*, 92, 095502, 2004. With permission.)

**FIGURE 8.8**

Si L EEL spectra obtained from an Si/SiO_2 interface compared to spectra from Si and SiO_2 far from the interface. Due to the high band gap in SiO_2 the edge onset is shifted higher in energy. The spectrum from the interface shows the presence of states in the band gap of SiO_2 indicating suboxide bonds. (Reproduced from Pennycook, S.J. et al., *Encyclopedia of Materials: Science and Technology*, Elsevier Science Ltd., Kidlington, Oxford, 2001 p. 1. With permission.)

**FIGURE 8.9**

Probe intensity distributions for three generations of STEM, (a) an uncorrected VG Microscopes HB501UX 100 kV STEM with depth of field \sim 45 nm, (b) the aberration-corrected HB603U 300 kV STEM with depth of field \sim 3.7 nm, and (c) for a next generation fifth-order aberration-corrected 200 kV microscope with predicted depth of field \sim 1 nm. Intensities are shown on a logarithmic scale and curves have been shifted vertically to locate maxima at zero defocus. (Reproduced from Borisevich, A.Y., Lupini, A.R., and Pennycook, S.J., *Proc. Nat. Acad. Sci. USA*, 103, 3044, 2006. With permission.)

smaller than the specimen thickness, as illustrated in Figure 8.9. This means that we are able to optically section the specimen, rather as in a confocal optical microscope. A through-focal series of images becomes a depth sequence of images, which can be reconstructed to obtain useful information on the three-dimensional structure of the object [9,10]. The sectioning is opposed by the tendency of a crystal to channel the electrons along atomic columns [60], and so the method works best in amorphous materials or, if aligned crystals are used, the columns should be weakly channeling, i.e., low Z.

For more detailed discussions on STEM and the benefits and applications of aberration correction the reader is referred to several recent reviews [32,34,37,61–63].

8.3 Theoretical Microscope

Density-functional total-energy calculations provide valuable complementary insight into atomic-scale structure and the only quantitative link to macroscopic properties. Theory can validate impurity or defect configurations seen in the microscope as stable, low-energy structures, and provide formation and migration energies, predict local electronic structure for comparison with EELS data, and, as we show later, even predict transport properties. This joint approach to understand structure and property relationships has proved fruitful in many semiconductor systems. In some cases theoretical

predictions stimulate experimental observations, while in other cases experiment comes first and theory provides the rationalization.

As an example of the additional insights available from complementary theory and experiment, we present the case of As-doped grain boundaries in Si. This began as a theoretical study motivated by the observation that experimental segregation energies for As in Si grain boundaries are around 0.5 eV; whereas, available theory predicted segregation energies of around 0.1 eV [64]. The reason for this discrepancy was soon found to be the assumption that impurities would be present in the boundary as isolated atoms. It was well known that grain boundaries in tetrahedrally coordinated semiconductors were fully rebonded, i.e., contained no dangling bonds. Priory theory assumed that As is incorporated in the grain boundary just like in the bulk, i.e., at isolated substitutional sites. The new hypothesis was that As dopants form pairs, each atom obtaining its preferred threefold configuration, as shown in Figure 8.10 [65]. The segregation energy per As atom increased threefold for certain sites. Z-contrast images of As in a Si grain boundary (see below) confirmed the formation of As pairs in certain sites, as predicted. It is the environment of the grain boundary that allows the As–As distance to increase,

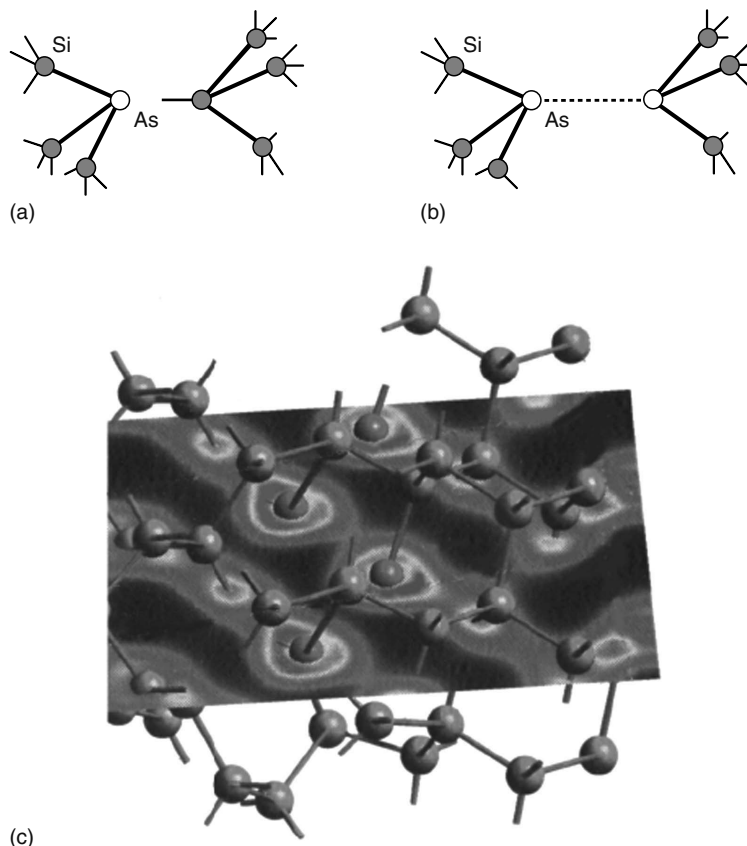
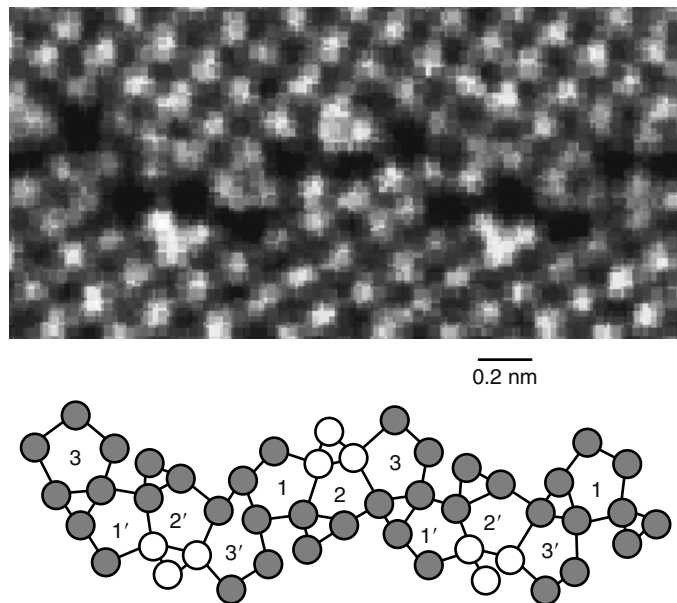


FIGURE 8.10

(a) Arsenic (As) prefers threefold coordination, so isolated As dopants create Si dangling bonds. (b) As dimers, however, can lower their energy by relaxing away from each other leaving no dangling bonds. This can only be accomplished in the grain boundary environment. (c) Plot showing the reduced charge density between the As dimers compared to between Si atoms. (Adapted from Maiti, A. et al., *Phys. Rev. Lett.*, 77, 1306, 1996. With permission.)

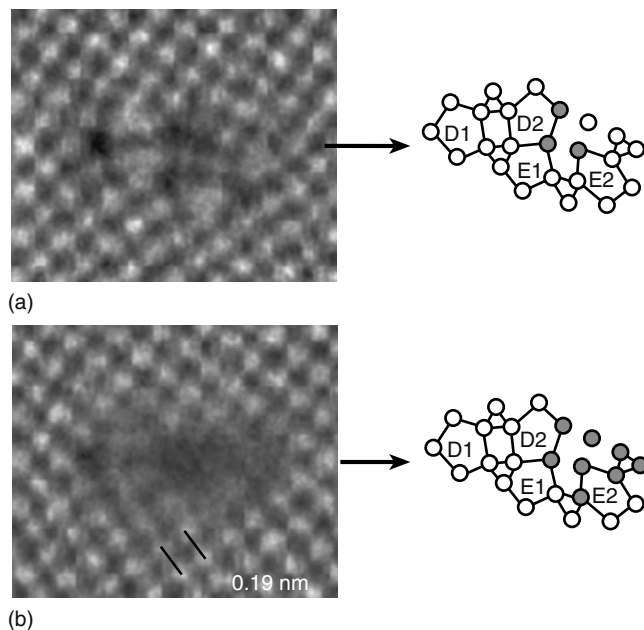
**FIGURE 8.11**

Z-contrast image of a $23^\circ \Sigma = 13\{510\} <001>$ tilt grain boundary in Si, with schematic diagram showing the boundary to comprise three dislocation cores which are then mirrored across the boundary plane. As is seen to segregate only to one of the three dislocation cores, seen as bright triangles in the image. Results obtained with the uncorrected HB603U. (Reproduced from Chisholm, M.F. et al., *Phys. Rev. Lett.*, 81, 132, 1998. With permission.)

allowing the repulsive energy of near neighbor As atoms to be avoided, an example of cooperative chemical rebonding. In the bulk crystal there is no such elastic relaxation. In fact, the energy of a dimer is slightly higher than that of two isolated atoms. Figure 8.10c shows the calculated charge density between the two atoms of an As dimer, showing it to be significantly reduced compared to that in the Si-Si bond.

The theory was performed on the lowest period grain boundary to minimize computational cost, a symmetric $\Sigma = 5\{310\} <001>$ tilt grain boundary, which has a misorientation of 36° . Later, experimental observations were made on a lower-angle grain boundary [66], a symmetric $23^\circ \Sigma = 13\{510\} <001>$ tilt grain boundary. The structure of this boundary was found to be surprisingly complex, as shown in Figure 8.11, comprising a contiguous array of six dislocation cores, a perfect edge dislocation (1), and two perfect mixed type dislocations (1,2) arranged as a dipole (i.e., their dislocation content cancels and they could be replaced by perfect crystal without changing the misorientation of the grain boundary). The same sequence is then mirrored across the boundary plane, denoted by primed numbers. The presence of As is revealed as a higher intensity in one of the two mixed type dislocation cores, repeated periodically along the boundary structure. Clearly, only two of the six cores forming the boundary structure contain As. The extra intensity in the image was about 18%, indicating an As concentration of about 5% per column, or about two As atoms in the specimen thickness. This image was obtained before aberration correction, and so single atom sensitivity was not possible for atoms of such low Z (33 for As compared to 14 for Si).

Theory was then performed on this more complex 23° boundary structure, but as with the 36° boundary, segregation energies for isolated As atoms never exceeded 0.1 eV. Although calculations for truly isolated As dimers could not be carried out because the required supercell would be too large, calculations for As chains (a continuous line of As

**FIGURE 8.12**

Z -contrast image of a $16^\circ \Sigma = 25\{710\} <001>$ tilt grain boundary in Si and derived structures with increasing electron irradiation. (a) With little electron irradiation only the three columns shaded show reduced intensity due to damage. (b) With increasing irradiation the damage spreads. Results obtained with the uncorrected HB603U. (Adapted from Maiti, A. et al., *Appl. Phys. Lett.*, 75, 2380, 1999. With permission.)

dimers) showed that only in core 2 was there significant segregation energy, in full accord with experiment. The theory showed further the reason for this. In cores 1 and 3, the relaxation of a dimer caused rotation toward the tilt axis, pushing the As atoms toward the neighboring dimer. In core 2, the relaxation rotated the dimer away from the tilt axis, allowing the As–As separation to increase, thereby lowering the energy. Thus the theory provides a perfect rationalization of the experimental observations, showing how it is the fine details of the boundary geometry that controls segregation, and specific sites can be favored to a significant degree.

Another example where theory rationalized microscopic observation is in the generation of vacancies by the fast electron beam. The observations were made on a lower-angle $16^\circ \Sigma = 25\{710\} <001>$ tilt grain boundary where the dislocations formed isolated, but still complex arrangements, as shown in Figure 8.12 [67]. Again, cores D1 and D2 represent a dipole, their dislocation content canceling, while cores E1 and E2 are mixed dislocations. With electron irradiation the intensity of specific columns shaded in the schematic decreased, indicating atomic displacements, the onset of amorphization. It was clear that the damage initiated in the vicinity of core E1. To explain these observations vacancy and interstitial formation energies were computed for various configurations. In the case of vacancies, all configurations in the boundary had much lower formation energies than in the bulk, as expected, but in particular, all the low-energy defect structures indeed occurred in the vicinity of the region seen dark in the micrograph. On the contrary, with interstitials, no correlation was found to the dark region of the image. It is clear therefore that the irradiation induces stable vacancy complexes; whereas, the ejected interstitials diffuse rapidly away.

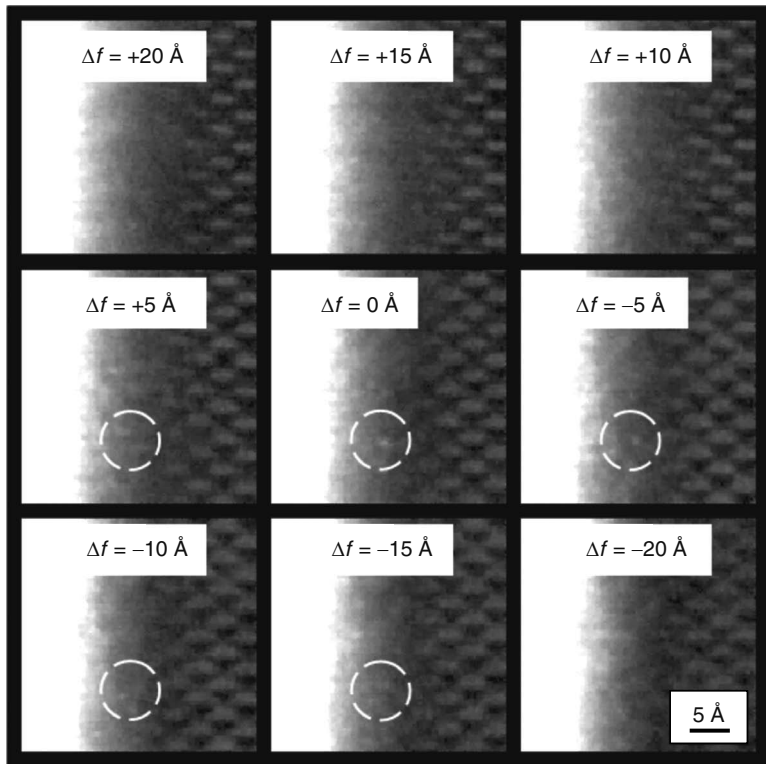
8.4 Structure and Properties of Si/SiO₂/HfO₂ Gate Stacks by Aberration-Corrected STEM and Theory

One of the more promising routes to overcome the potential “end of the roadmap” for shrinking Si-based devices is to move to alternative gate dielectrics with higher dielectric constant, the so-called high-*k* dielectrics, of which HfO₂ is perhaps the most widely studied material (Chapters 9 through 14). The high-*k* gives a smaller effective dielectric thickness, but introduces new concerns. Key issues include whether the Si/SiO₂ interface remains well-passivated or whether Hf atoms would segregate to the interface and degrade its characteristics through introduction of localized states, either directly or through introduction of dangling bonds. Localized states could act as scattering centers for electrons moving in the channel, reducing mobility, or, at a sufficiently high density, might enable leakage through the thin SiO₂ layer. To investigate these effects, aberration-corrected STEM combined with theory is emerging as a powerful combination, providing the ability to locate single Hf atoms in three dimensions within the gate oxide, and through theory, to predict macroscopic properties.

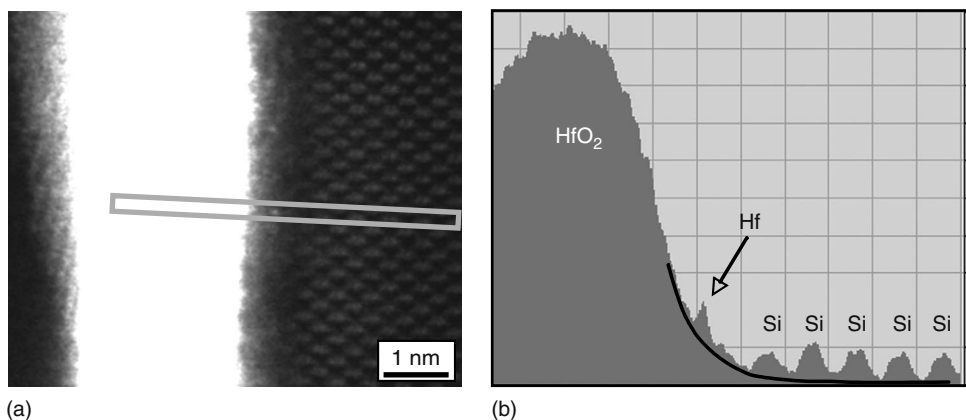
One of the most important advantages of the short depth of focus in the aberration-corrected microscope is with the probe focused inside the specimen; atoms on the top and bottom surfaces are out of focus, and hence invisible. Therefore, a through focal series ensures that Hf atoms inside the actual device structure are indeed being examined, with no possibility of the atoms being part of any surface layers produced during specimen preparation. For the present study, HfO₂ films approximately 3 nm thick were deposited on silicon substrates by atomic layer deposition, and then rapid thermally annealed at 950°C for 30 s in N₂. The films were then capped with undoped polycrystalline Si. Samples were prepared purely by mechanical polishing to avoid damaging the thinnest regions by ion milling. Part of a through focal series of images is shown in Figure 8.13, in which a bright spot is clearly seen at a defocus of zero and -5 Å, but fades at lower or higher defocus. A line trace across such an image is shown in Figure 8.14, revealing that the excess intensity of the Hf atom is comparable to that of an entire column of Si atoms, which is in agreement with image simulations [8,10]. This rules out the possibility that the spots could be due to a lighter element such as Zr, a known possible impurity in these systems. It is also apparent that the intensity across the oxide is highly nonuniform, which represents the out of focus contributions of other Hf atoms and particularly the HfO₂ at other depths. Because of this out of focus background, the atoms are only visible when in sharp focus. Figure 8.15 shows plots of the excess intensity extracted from such line traces for a few representative atoms as a function of focus, or atom depth. The plot clearly shows how the depth of the Hf atoms can be determined to a precision of much better than ±0.5 nm, just by locating the position of the peak intensity. For atoms that are widely separated, as in the present example, the depth precision therefore significantly exceeds the expected depth resolution. The specimen thickness is assumed to be approximately equal to the greatest difference in depth found between Hf atoms, in this case 6 nm.

A total of 65 atoms were analyzed in this focal series which were randomly distributed in depth. Interestingly, their lateral position was not found to be random. The lateral precision is an order of magnitude greater than the depth precision, at a level of 0.1 nm or higher limited primarily by specimen drift. Figure 8.16a shows an image with positions of some Hf atoms marked, along with a histogram of the lateral positions with respect to the interface plane. No Hf atoms are present right at the interface, and they prefer to sit at specific distances from the interface, around 2.5 and 4 Å.

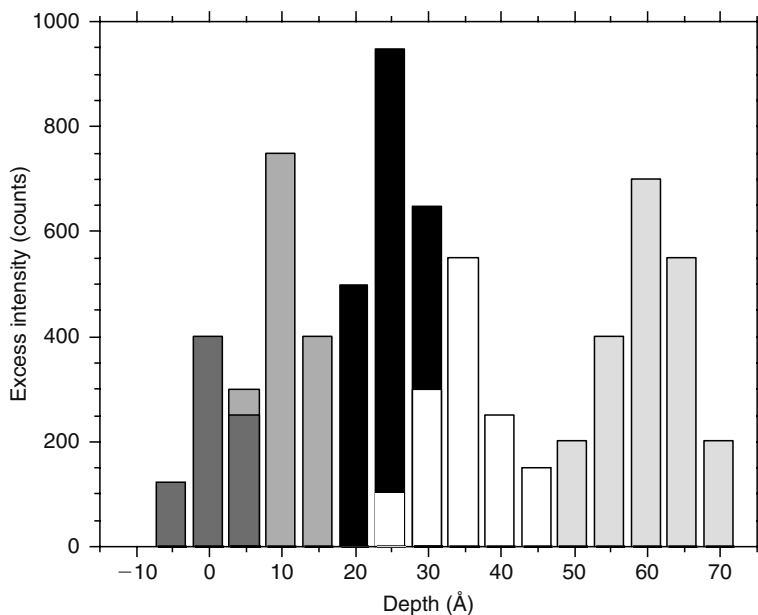
Now it is obvious that a transition from crystalline Si to a truly disordered oxide cannot occur instantaneously, and some order is therefore expected right near to the last Si plane.

**FIGURE 8.13**

Sequence of frames from a through-focal series of Z-contrast images of an Si/SiO₂/HfO₂ high-*k* device structure showing an individual Hf atom coming in and out of focus (circled). Results obtained with the aberration-corrected HB603U. (Adapted from van Benthem, K. et al., *Appl. Phys. Lett.*, 87, 034104, 2005. With permission.)

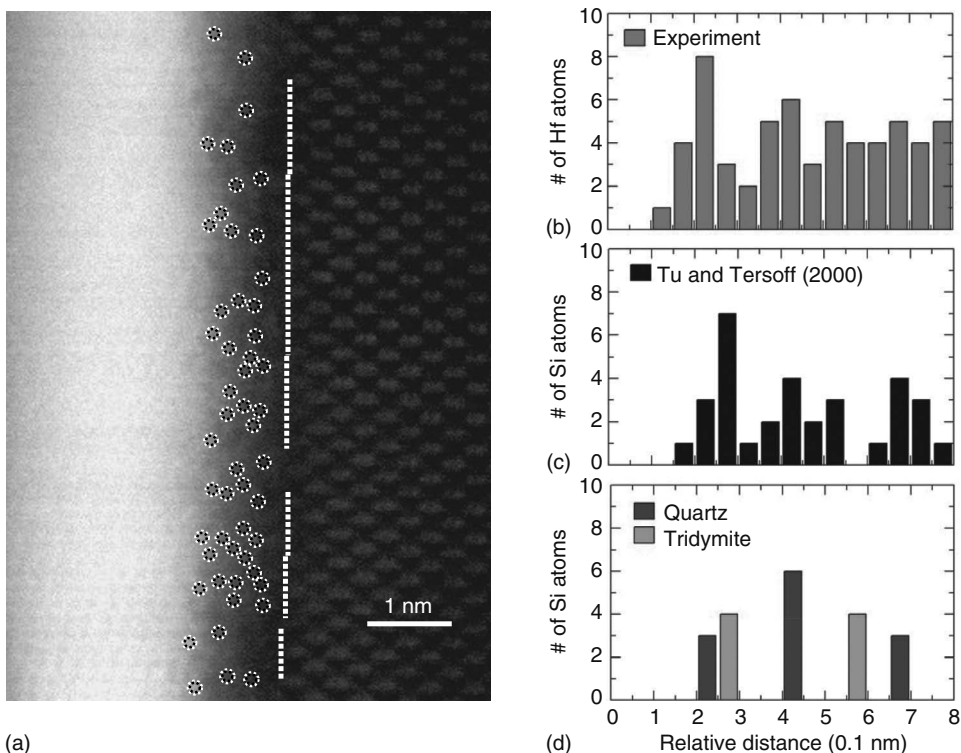
**FIGURE 8.14**

(a) One frame from the through-focal series showing a single atom with an intensity profile taken from the rectangular box (b) showing a large nonuniform background contribution. (Adapted from van Benthem, K. et al., *Ultramicroscopy*, 106, 1062, 2006. With permission.)

**FIGURE 8.15**

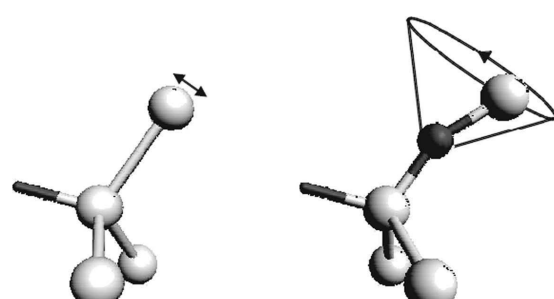
Plot showing the excess intensity from several individual Hf atoms as a function of depth. (Adapted from van Benthem, K. et al., *Ultramicroscopy*, 106, 1062, 2006. With permission.)

None is apparent in the Z-contrast image, however, and so we turn to theory. Several studies of the Si/SiO₂ interface have been carried out, and here we compare the experimental data to two studies, the first to a study without Hf using classical potentials [68] with a large number of atoms, and the second to density functional calculations including Hf, using by necessity a smaller number of atoms [69]. The classical potential calculations give a fair reproduction of the experimental Hf histogram (see Figure 8.16b and c), therefore suggesting that the Hf atoms substitute for Si in the oxide. This was tested explicitly by density functional theory using various crystalline models for the interface studied previously. In that work it was found energetically preferable to have abrupt interfaces, avoiding suboxide bonds [69]. The rationalization of this result was that Si–Si bonds are stiff, and the structural mismatch at the interface can be better accommodated by inserting an oxygen atom into any Si–Si bond that may protrude into the oxide. A Si–O–Si bond has a soft angle at the O atom that allows the bond angle to vary, as shown in Figure 8.17. Two particular oxide structures were found to have the lowest energy, tridymite-like bonding and quartz-like bonding. Quartz-like bonding results in tension in the oxide, in the plane of the interface, whereas tridymite-like bonding results in compression. It was therefore concluded that the actual interface structure would most likely consist of an intimate phase mixture of these two types of bonding to avoid any long-range elastic strains. We therefore looked at the two models to extract the distance from the interface plane to the first Si atoms, and found 2.3 and 4.4 Å for the quartz-like structure, and longer distances for the crystobalilte-like structure, 2.9 and 5.4 Å. Inserting these distances onto a histogram, we find that the result is also in reasonable agreement with the data (Figure 8.16d). Furthermore, the theory directly confirmed that substitutional Hf is preferred over interstitial Hf, by at least 4 eV [70]. Interstitial Hf results in disruption of the oxide lattice, because the Hf atoms steal O atoms from the Si leading to the creation of dangling bonds. Comparing the energy of substitutional Hf in different

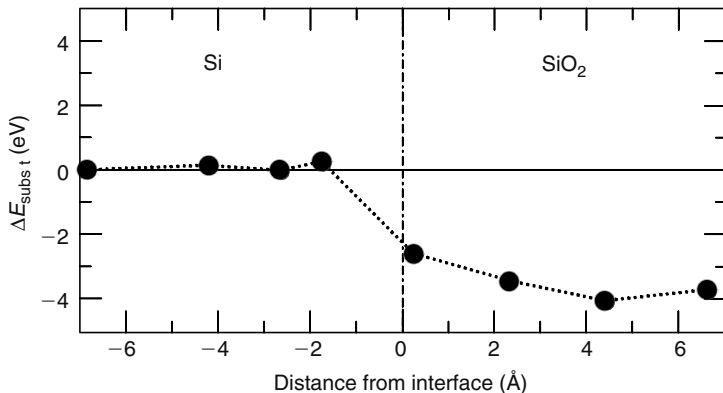
**FIGURE 8.16**

(a) Image of the device structure with Hf atom positions superimposed. No Hf atoms are found at the Si/SiO₂ interface. (b) Histogram showing the distance of Hf atoms from the Si/SiO₂ interface compared to (c) Si positions obtained by classical potential calculations (courtesy J. Tersoff) and (d) first-principles calculations of model abrupt interfaces to crystalline SiO₂. (Adapted from Marinopoulos, A.G. et al., *Phys. Rev. B* 77, 195317, 2008. With permission.)

sites also explains why the Hf atoms keep away from the interface. Figure 8.18 shows a plot of the energy of formation for substitutional Hf, taking the zero to be in bulk Si, which shows how the Hf prefers the more open oxide structure, where it can have O neighbors, and even how it prefers to stay away from the interface plane by a significant energy, 1.4 eV. Also, since the source of the Hf atoms is the HfO₂, we would not expect Hf to migrate into the Si substrate. Thus, the theory completely explains all the

**FIGURE 8.17**

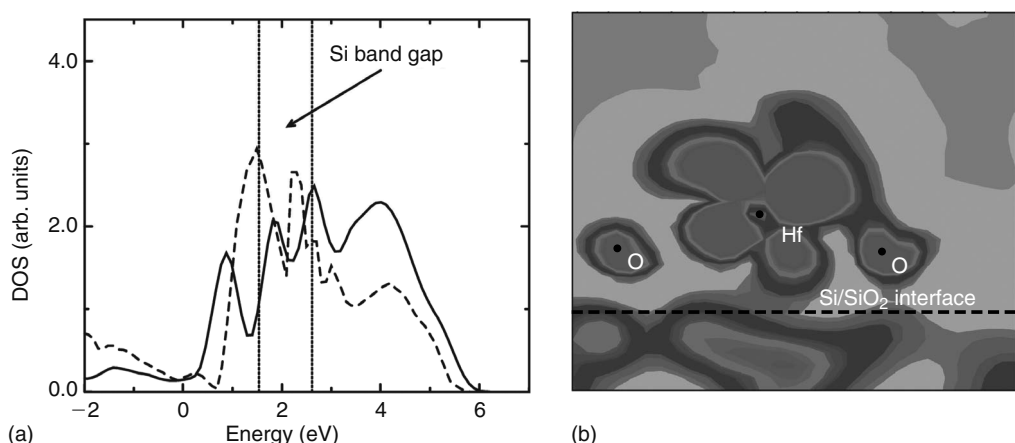
Schematic diagram showing the additional degree of freedom obtained with an Si-O-Si bond compared to the stiff Si-Si bond. (Reproduced from Buczko, R., Pennycook, S.J., and Pantelides, S.T., *Phys. Rev. Lett.*, 84, 943, 2000. With permission.)

**FIGURE 8.18**

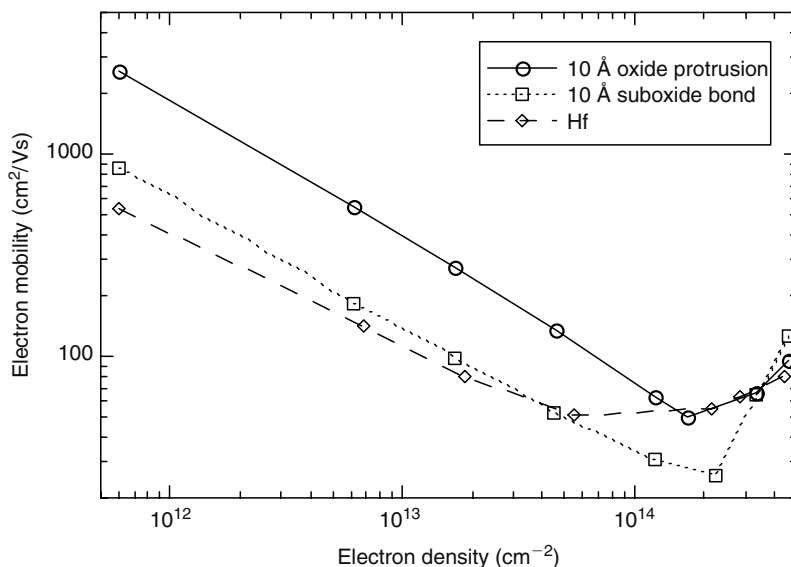
Plot showing the formation energy for substitutional Hf atoms across the interface. Hf atoms at the interface have 1.4 eV higher energy than those in the oxide, explaining why none were found in that position. (Adapted from Marinopoulos, A.G. et al., *Phys. Rev. B* 77, 195317, 2008. With permission.)

experimental observations leading to a detailed microscopic explanation of the structure and energetics of the system.

Theory also gives insight into the electronic properties of the material. In Figure 8.19, we plot the densities of states around two interstitial configurations of Hf showing how they overlap the Si band gap and are therefore electrically active. Also shown is the wave function of the 4d localized state, along with the wave function of the bottom of the Si conduction band, showing a significant lateral extent overlapping the neighboring O and Si atoms. Substitutional Hf showed similar behavior. From the data shown in Figure 8.16, knowing the coordinates of all the atoms it is simple to deduce their density, 1.4 nm^{-3} ($1.7 \times 10^{14} \text{ cm}^{-2}$), and hence determine their average separation to be about 7 Å. It is clear

**FIGURE 8.19**

(a) Densities of states around two interstitial Hf atoms overlap the Si band gap. (b) Plot of the Hf 4d localized state, and the wave function of the bottom of the Si conduction band, showing a significant lateral extent. (Adapted from Pantelides, S.T. et al., *NATO Advanced Research Workshop on Defects in High-K Dielectrics and Nano-Electronic Semiconductor Devices*, Russia, 2005. With permission.)

**FIGURE 8.20**

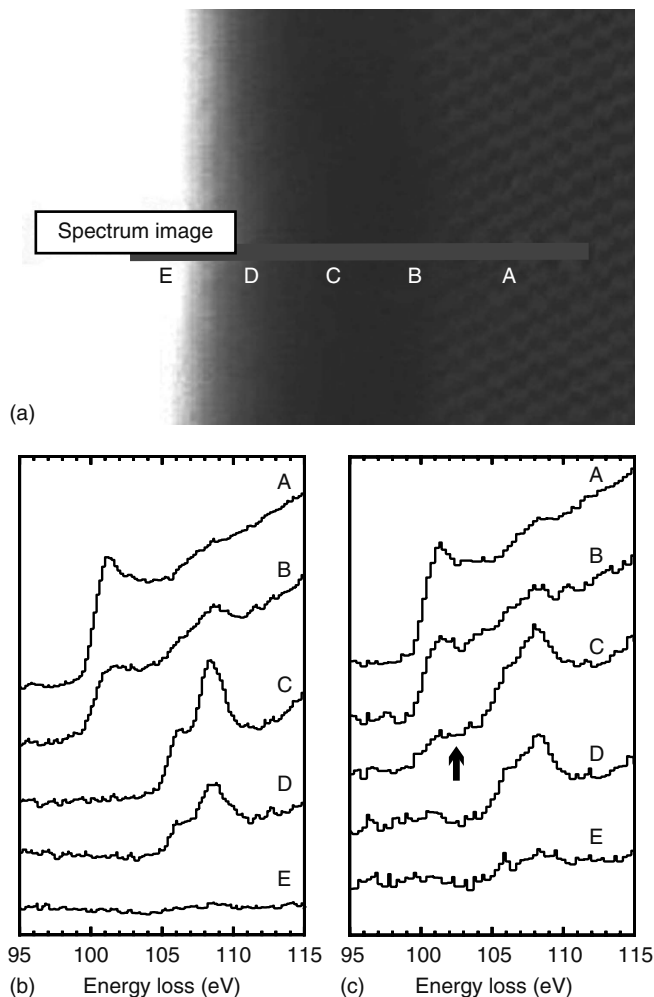
Electron mobilities for a variety of defects at an Si/SiO₂ interface calculated by first principles. (Data taken from Evans, M.H. et al., *Phys. Rev. Lett.*, 95, 106802, 2005; Evans, M.H. et al., *IEDM Tech. Dig.*, 597, 2005. With permission.)

that at this density their wave functions could overlap significantly and explain the high leakage observed in this particular sample.

Mobilities can also be determined from first principles, by calculating a scattering potential as the difference between a perfect interface and one containing the defect of interest, a suboxide bond, an oxide protrusion, and a Hf atom [71]. Results for these defects are compared in Figure 8.20, and it is clear that the Hf atoms do represent a large potential contribution to mobility reduction in these thin gate oxide structures [72].

8.5 Future Directions

The aberration-corrected results presented here were all using third-order correctors, which correct for geometric aberrations up to third order, leaving the resolution-limiting aberrations to be of fifth order. However, correctors are in development that will correct the fifth-order aberrations, leaving resolution-limiting aberrations to be of seventh order, which would allow roughly another factor of 2 in aperture angle [73,74]. We can look forward to further improved resolution (in principle, another factor of 2, assuming that other factors do not come into play such as instabilities) and a factor of 4 in depth resolution, approaching a depth resolution of 1 nm [9]. Again, we can expect sensitivities for individual atoms to improve, and all benefits will apply not only to the image but also to EELS. In principle, we should be able to probe electronic structure around individual Hf atoms with a depth resolution that is not much larger than the extent of the wave function seen in Figure 8.19, and a through depth sequence of EELS data could be used to isolate the contribution from the region of the Hf atom. An indication of the possibilities is seen in

**FIGURE 8.21**

(a) Z-contrast image of an Si/SiO₂/HfO₂ high-*k* device structure showing regions analyzed by EELS (b) before and (c) after rapid thermal annealing, which introduced stray Hf atoms and a significant density of states in the region of the Si band gap (arrowed).

Figure 8.21, which shows EELS spectra from various regions of the gate stack before and after rapid thermal annealing. Before annealing, no Hf atoms were seen in the SiO₂, but they were present after annealing at a density of 0.3 Hf nm⁻³ in this case. The EELS data show that the density of states within the Si band gap increased substantially after annealing, suggesting a correlation with the presence of Hf. Such ideas could be tested directly with the improved three-dimensional resolution available with next generation STEM instruments.

Acknowledgments

The authors are grateful to many colleagues for the collaborations mentioned in this article, including A.R. Lupini, A.Y. Borisevich, M. Varela, P.D. Nellist, O.L. Krivanek, N. Dellby,

M.F. Murfitt, Z.S. Szilagyi, S.N. Rashkeev, S.F. Findlay, M.P. Oxley, L.J. Allen, H.M. Christen, G. Duscher, A. Maiti, M. Kim, H.S. Baik, R. Buczko, S.N. Rashkeev, M.H. Evans, W.H. Sides, and J.T. Luck. Work at Oak Ridge National Laboratory (ORNL) was supported by the Division of Materials Science and Engineering (S.J.P., M.F.C., K.v.B., S.T.P.), at Vanderbilt by the Air Force Office of Scientific Research under a MURI grant (FA9550-05-1-0306), the National Science Foundation grant ECS-0524655, and by the McMinn Endowment at Vanderbilt University (A.G.M., S.T.P.), also by appointments to the ORNL postdoctoral program (K.v.B.) and distinguished visiting scientist program (S.T.P.) administered jointly by ORNL and Oak Ridge Institute for Science and Education, and by a fellowship from the Alexander-von-Humboldt Foundation (K.v.B.). Theoretical work was supported in part by a grant of computer time from the DoD High Performance Computing Modernization Program at Maui High Performance Computer Center and U.S. Army Engineer Research and Development Center.

References

1. Rose, H., Correction of aberrations, a promising means for improving the spatial and energy resolution of energy-filtering electron microscopes, *Ultramicroscopy* 56, 11, 1994.
2. Scherzer, O., Das theoretisch erreichbare Auflösungsvermögen des Elektronenmikroskops, *Z. Physik* 114, 427, 1939.
3. Feynman, R.P., There's plenty of room at the bottom, available at Caltech, 1959, available at <http://www.its.caltech.edu/~feynman/plenty.html>
4. Scherzer, O., Sparische und chromatische Korrektur von Electronen-Linsen, *Optik* 2, 114, 1947.
5. Haider, M. et al., A spherical-aberration-corrected 200 kV transmission electron microscope, *Ultramicroscopy* 75, 53, 1998.
6. Batson, P.E., Dellby, N., and Krivanek, O.L., Sub-angstrom resolution using aberration corrected electron optics, *Nature* 418, 617, 2002.
7. Nellist, P.D. et al., Direct sub-angstrom imaging of a crystal lattice, *Science* 305, 1741, 2004.
8. van Benthem, K. et al., Three-dimensional imaging of individual hafnium atoms inside a semiconductor device, *Appl. Phys. Lett.* 87, 034104, 2005.
9. Borisevich, A.Y., Lupini, A.R., and Pennycook, S.J., Depth sectioning with the aberration-corrected scanning transmission electron microscope, *Proc. Nat. Acad. Sci. USA* 103, 3044, 2006.
10. van Benthem, K. et al., Three-dimensional ADF imaging of individual atoms by through-focal series scanning transmission electron microscopy, *Ultramicroscopy* 106, 1062, 2006.
11. Cowley, J.M., Image contrast in a transmission scanning electron microscope, *Appl. Phys. Lett.* 15, 58, 1969.
12. Pennycook, S.J. and Jesson, D.E., High-resolution incoherent imaging of crystals, *Phys. Rev. Lett.* 64, 938, 1990.
13. Pennycook, S.J. and Jesson, D.E., High-resolution Z-contrast imaging of crystals, *Ultramicroscopy* 37, 14, 1991.
14. Jesson, D.E., Pennycook, S.J., and Baribeau, J.M., Direct imaging of interfacial ordering in ultra-thin $(\text{Si}_m\text{Ge}_n)_P$ superlattices, *Phys. Rev. Lett.* 66, 750, 1991.
15. Pennycook, S.J. and Jesson, D.E., Atomic resolution Z-contrast imaging of interfaces, *Acta Metall. Mater.* 40, S149, 1992.
16. Pennycook, S.J. et al., Atomic-resolution imaging and spectroscopy of semiconductor interfaces, *Appl. Phys. A* 57, 385, 1993.
17. Chisholm, M.F. et al., Z-contrast investigation of the ordered atomic interface of $\text{CoSi}_2/\text{Si}(001)$ layers, *Appl. Phys. Lett.* 64, 3608, 1994.
18. Chisholm, M.F. et al., New interface structure for a-type $\text{CoSi}_2/\text{Si}(111)$, *Appl. Phys. Lett.* 64, 2409, 1994.
19. McGibbon, A.J., Pennycook, S.J., and Angelo, J.E., Direct observation of dislocation core structures in $\text{CdTe}/\text{GaAs}(001)$, *Science* 269, 519, 1995.

20. Pennycook, S.J. et al., Direct determination of interface structure and bonding with the scanning transmission electron microscope, *Philos. Trans. R. Soc. London Ser. A* 354, 2619, 1996.
21. James, E.M. and Browning, N.D., Practical aspects of atomic resolution imaging and analysis in STEM, *Ultramicroscopy* 78, 125, 1999.
22. Dellby, N. et al., Progress in aberration-corrected scanning transmission electron microscopy, *J. Electron Microsc.* 50, 177, 2001.
23. Krivanek, O.L., Dellby, N., and Lupini, A.R., Towards sub-angstrom electron beams, *Ultramicroscopy* 78, 1, 1999.
24. Abe, E., Pennycook, S.J., and Tsai, A.P., Direct observation of a local thermal vibration anomaly in a quasicrystal, *Nature* 421, 347, 2003.
25. Pennycook, S.J. et al., Aberration-corrected scanning transmission electron microscopy: The potential for nano- and interface science, *Z. Metallkd.* 94, 350, 2003.
26. Varela, M. et al., Nanoscale analysis of $\text{YBa}_2\text{Cu}_3\text{O}_{7-x}/\text{La}_{0.67}\text{Ca}_{0.33}\text{MnO}_3$ interfaces, *Solid State Electron.* 47, 2245, 2003.
27. McBride, J.R. et al., Aberration-corrected Z-contrast scanning transmission electron microscopy of CdSe nanocrystals, *Nano Lett.* 4, 1279, 2004.
28. Shibata, N. et al., Observation of rare-earth segregation in silicon nitride ceramics at subnanometre dimensions, *Nature* 428, 730, 2004.
29. Wang, S.W. et al., Dopants adsorbed as single atoms prevent degradation of catalysts, *Nat. Mater.* 3, 274, 2004.
30. Klie, R.F. et al., Enhanced current transport at grain boundaries in high-Tc superconductors, *Nature* 435, 475, 2005.
31. Prabhumirashi, P. et al., Atomic-scale manipulation of potential barriers at SrTiO_3 grain boundaries, *Appl. Phys. Lett.* 87, 121917, 2005.
32. Varela, M. et al., Materials characterization in the aberration-corrected scanning transmission electron microscope, *Annu. Rev. Mater. Res.* 35, 539, 2005.
33. Chisholm, M.F. and Pennycook, S.J., Direct imaging of dislocation core structures by Z-contrast STEM, *Philos. Mag.* 86, 4699, 2006.
34. Pennycook, S.J. et al., Materials advances through aberration-corrected electron microscopy, *MRS Bull.* 31, 36, 2006.
35. Varela, M. et al., Atomic scale characterization of complex oxide interfaces, *J. Mater. Sci.* 41, 4389, 2006.
36. Shibata, N. et al., Nonstoichiometric dislocation cores in alpha-alumina, *Science* 316, 82, 2007.
37. Pennycook, S.J., Microscopy: Transmission electron microscopy, in *Encyclopedia of Condensed Matter Physics*, Bassani, F., Liedl, J., and Wyder, P., Eds., Elsevier Science Ltd., Kidlington, Oxford, 2006, p. 240.
38. Rashkeev, S.N. et al., Single Hf atoms inside the ultrathin SiO_2 interlayer between a HfO_2 dielectric film and the Si substrate: How do they modify the interface? *Microelectron. Eng.* 80, 416, 2005.
39. van Benthem, K., Rashkeev, S.N., and Pennycook, S.J., Atomic and electronic structure investigations of $\text{HfO}_2/\text{SiO}_2/\text{Si}$ gate stacks using aberration-corrected STEM, in *Characterization and Metrology for ULSI Technology 2005*, Seiler, D.G., Diebold, A.C., McDonald, R., Ayre, C.R., Khosla, R.P., Zollner, S., and Secula, E.M., Eds., American Institute of Physics, Richardson, TX, 2005, p. 79.
40. Diebold, A.C. et al., Thin dielectric film thickness determination by advanced transmission electron microscopy, *Microsc. Microanal.* 9, 493, 2003.
41. Hytch, M.J. and Stobbs, W.M., Quantitative comparison of high-resolution TEM images with image simulations, *Ultramicroscopy* 53, 191, 1994.
42. Browning, N.D., Chisholm, M.F., and Pennycook, S.J., Atomic-resolution chemical-analysis using a scanning-transmission electron-microscope, *Nature* 366, 143, 1993.
43. Browning, N.D. and Pennycook, S.J., Atomic-resolution electron energy-loss spectroscopy in the scanning transmission electron microscope, *J. Microsc.-Oxford* 180, 230, 1995.
44. Browning, N.D. et al., EELS in the STEM: Determination of materials properties on the atomic scale, *Micron* 28, 333, 1997.
45. Dickey, E.C. et al., Structure and bonding at Ni-ZrO₂ (cubic) interfaces formed by the reduction of a NiO-ZrO₂ (cubic) composite, *Microsc. Microanal.* 3, 443, 1997.

46. Duscher, G., Browning, N.D., and Pennycook, S.J., Atomic column resolved electron energy-loss spectroscopy, *Phys. Stat. Solidi A* 166, 327, 1998.
47. Pennycook, S.J. et al., A combined experimental and theoretical approach to grain boundary structure and segregation, *Physica B* 274, 453, 1999.
48. Rafferty, B. and Pennycook, S.J., Towards atomic column-by-column spectroscopy, *Ultramicroscopy* 78, 141, 1999.
49. Varela, M. et al., Spectroscopic imaging of single atoms within a bulk solid, *Phys. Rev. Lett.* 92, 095502, 2004.
50. Bosman, M., Two-dimensional mapping of chemical information at atomic resolution, *Phys. Rev. Lett.* 99, 086102, 2007.
51. Pennycook, S.J. et al., Dislocations in semiconductors: atomic structure and properties, in *Encyclopedia of Materials: Science and Technology*, Mahajan, S. and Narayan, Eds., J. Elsevier Science Ltd, Kidlington, Oxford, 2001, p. 1.
52. Arslan, I. et al., Atomic and electronic structure of mixed and partial dislocations in GaN, *Phys. Rev. Lett.* 94, 025504, 2005.
53. Arslan, I. and Browning, N.D., Intrinsic electronic structure of threading dislocations in GaN, *Phys. Rev. B* 65, 075310, 2002.
54. Arslan, I. and Browning, N.D., Role of oxygen at screw dislocations in GaN, *Phys. Rev. Lett.* 91, 165501, 2003.
55. Buczko, R. et al., Excitonic effects in core-excitation spectra of semiconductors, *Phys. Rev. Lett.* 85, 2168, 2000.
56. Chisholm, M.F. et al., Atomic structure and properties of extended defects in silicon, *Solid State Phenom.* 67–68, 3, 1999.
57. Stemmer, S. et al., Stability of ZrO₂ layers on Si (001) during high-temperature anneals under reduced oxygen partial pressures (vol. 92, p. 82, 2002), *J. Appl. Phys.* 92, 6942, 2002.
58. Stemmer, S. et al., Electron energy-loss spectroscopy study of thin film hafnium aluminates for novel gate dielectrics, *J. Microsc.-Oxford* 210, 74, 2003.
59. Stemmer, S. et al., Reactions of Y₂O₃ films with (001) Si substrates and with polycrystalline Si capping layers, *Appl. Phys. Lett.* 81, 712, 2002.
60. Borisevich, A.Y. et al., Depth sectioning of aligned crystals with the aberration-corrected scanning transmission electron microscope, *J. Electron Microsc.* 55, 7, 2006.
61. Pennycook, S.J. and Nellist, P.D., Z-contrast scanning transmission electron microscopy, in *Impact of Electron and Scanning Probe Microscopy on Materials Research*, Rickerby, D.G., Valdré, U., and Valdré, G., Eds., Kluwer Academic Publishers, Dordrecht, the Netherlands, 1999, p. 161.
62. Pennycook, S.J., Structure determination through Z-contrast microscopy, in *Advances in Imaging and Electron Physics*, Merli, P.G., Calestani, G., and Vittori-Antisari, M., Eds., Elsevier Science, New York, 2002, p. 173.
63. Nellist, P.D. and Pennycook, S.J., The principles and interpretation of annular dark-field Z-contrast imaging, in *Advances in Imaging and Electron Physics*, Kazan, B., Mulvey, T., and Hawkes, P., Eds., Elsevier, New York, 2000, p. 147.
64. Arias, T.A. and Joannopoulos, J.D., Electron trapping and impurity segregation without defects—ab-initio study of perfectly rebonded grain-boundaries, *Phys. Rev. B* 49, 4525, 1994.
65. Maiti, A. et al., Dopant segregation at semiconductor grain boundaries through cooperative chemical rebonding, *Phys. Rev. Lett.* 77, 1306, 1996.
66. Chisholm, M.F. et al., Atomic configurations and energetics of arsenic impurities in a silicon grain boundary, *Phys. Rev. Lett.* 81, 132, 1998.
67. Maiti, A. et al., Damage nucleation and vacancy-induced structural transformation in Si grain boundaries, *Appl. Phys. Lett.* 75, 2380, 1999.
68. Tu, Y. and Tersoff, J., Structure and energetics of the Si–SiO₂ interface, *Phys. Rev. Lett.* 84, 4393, 2000.
69. Buczko, R., Pennycook, S.J., and Pantelides, S.T., Bonding arrangements at the Si–SiO₂ and SiC–SiO₂ interfaces and a possible origin of their contrasting properties, *Phys. Rev. Lett.* 84, 943, 2000.

70. Marinopoulos, A.G. et al., Impurity segregation and ordering in Si/SiO₂/HfO₂ structures, *Phys. Rev. B* 77, 195317, 2008.
71. Evans, M.H. et al., First-principles mobility calculations and atomic-scale interface roughness in nanoscale structures, *Phys. Rev. Lett.* 95, 106802, 2005.
72. Evans, M.H. et al., First-principles modeling of double-gate UTSOI MSOFETs, *IEDM Tech. Dig.* 597, 2005.
73. Haider, M., Uhlemann, S., and Zach, J., Upper limits for the residual aberrations of a high-resolution aberration-corrected STEM, *Ultramicroscopy* 81, 163, 2000.
74. Krivanek, O.L. et al., Towards sub-0.5 angstrom electron beams, *Ultramicroscopy* 96, 229, 2003.

